International Journal of Solids and Structures 46 (2009) 1373–1388

Contents lists available at ScienceDirect

International Journal of Solids and Structures

journal homepage: www.elsevier.com/locate/ijsolstr

Microstructural modelling of stress-dependent behaviour of clay

Zhen-Yu Yin *, Ching S. Chang

Department of Civil and Environmental Engineering, University of Massachusetts, Amherst, MA 01002, USA

ARTICLE INFO

Article history:
Received 13 July 2008
Received in revised form 27 September 2008
Available online 17 November 2008

Keywords:
Anisotropy
Clays
Micromechanics
Constitutive relations
Plasticity
Stress reversal

ABSTRACT

The purpose of this paper is to investigate the stress-dependent behaviour of clay during drained and undrained shearing by means of a micromechanical approach. A new micromechanical stress–strain model is developed for clay using the approach developed in earlier studies by Chang and Hicher [Chang, C.S., Hicher, P.Y., 2005. An elastic–plastic model for granular materials with microstructural consideration. International Journal of Solids and Structures 42(14), 4258–4277]. In order to model the extension test on a K_0 consolidated sample, a formulation is developed to account for the stress reversal on a contact plane. The model is then used to simulate numerous stress-path tests on Lower Cromer Till and kaolin clay, including triaxial compression and extension tests, under both undrained and drained conditions, with different K_0 consolidation, and different over-consolidation ratios. The applicability of the present model is evaluated through comparisons between the predicted and the measured results. The evolution of local stresses and local strains at inter-particle planes are discussed in order to explain the stress-induced anisotropy due to externally applied load. All simulations have demonstrated that the proposed micromechanical approach is capable of modelling the stress-induced anisotropy and other major features of the complex behaviour in clay.

1. Introduction

Natural clay often exhibits significant anisotropic behaviour that may be either caused by the clay's fabric structure (inherent structural anisotropy) or induced as a result of stress change (stress-induced anisotropy). The fabric structure is usually created during the geological formation process of a clay deposit, in which the long axis of the soil particles tends to align in a preferred direction, thus generating the inherent structural anisotropy. However, clay can still exhibit anisotropic behaviour even through its fabric structure is isotropic. This type of anisotropic behaviour is induced by the *in situ* stress and subsequent loading conditions (e.g., see the work by Tavenas and Lereoueil, 1977; Muir Wood, 1990; Burland, 1990; Diaz Rodriguez et al., 1992). These studies have shown that the behaviour of clay is highly stress-dependent in nature. Therefore, clay always displays some degree of anisotropy under external loads. For this reason, it is important for a stress–strain model to have the capability of predicting stress-induced anisotropy.

The models that account for stress-induced anisotropy have been developed mainly through the elasto-plastic approach, such as Nova (1985), Dafalias (1986), Whittle and Kavvadas (1994), Pestana and Whittle (1999), Ling et al. (2002), Wheeler et al. (2003), Dafalias et al. (2006), etc. The key feature of these models is a kinematic hardening rule which describes how the yield surface moves and expands in accordance with the applied stresses. The kinematic hardening rule, constructed phenomenologically from experimental results, can simulate the phenomenon of stress-induced anisotropy. However, it is not an easy task to facilitate a kinematic hardening rule for the complex behaviour of soil.

Another interesting approach for modelling stress-induced anisotropy is the micro-structural model. This approach embraces slip plasticity models (Batdorf and Budianski, 1949; Calladine, 1971), multi-laminate models (Pande and Sharma, 1982; Cudny and Vermeer, 2004) and micro-plane models (Bazant et al., 1995). In this approach, material is considered as a collection of slip planes in different orientations. The stresses on each plane are considered as internal state variables, and their evolution can serve to model the behaviour change on each individual plane. Since the properties are stress-dependent, the results exhibit naturally the stress-induced anisotropy.

Although conceptually, the micro-structural approach is potentially attractive for modelling anisotropic material, it has not been evaluated for natural clay with complex behaviour under various stress paths in both drained and undrained conditions. For this purpose, we have developed a micromechanical model extended from the micro-structural approach of Chang and Hicher (2005) to study the induced anisotropy in natural soft clay. The macro behaviour of clay is very different from

* Corresponding author. Tel.: +1 413 545 5401; fax: +1 413 545 4525.
E-mail addresses: zhenyu.yin@gmail.com (Z.-Y. Yin), chang@ecs.umass.edu (C.S. Chang).

0020-7683/$ - see front matter © 2008 Elsevier Ltd. All rights reserved.
doi:10.1016/j.ijsolstr.2008.11.006

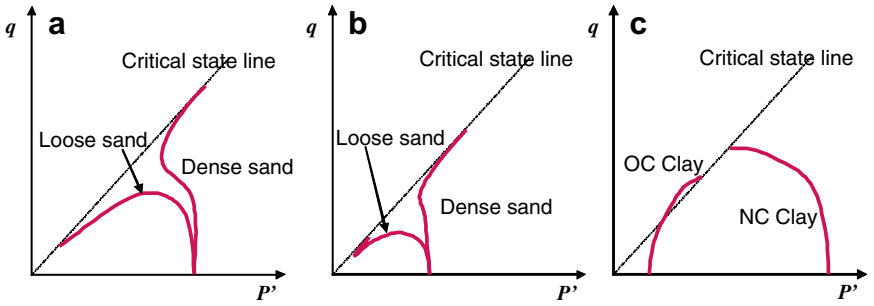

Fig. 1. Schematic plot for undrained compression behaviour of sand and clay: (a) under high confining pressure, (b) under low confining pressure, and (c) for NC and OC clay (NC, normally consolidated; OC, overconsolidated).

sand. For example, the critical state line in e-log p' plane is always parallel to the compression line for clay, whereas this is not necessarily true for sand. Furthermore, undrained experiments show very different nature in stress paths. Fig. 1 shows the schematic plot for undrained paths of sand and clay. Fig. 1a and b shows the behaviour of sand under high and low confining pressures, respectively. Fig. 1c shows the undrained stress paths for both normally consolidated and heavily overconsolidated clay. Near critical state, the undrained paths for sand have pronounced behaviours of contraction and dilation (up-turn or down-turn), whereas the undrained paths for clay do not have such behaviour. Furthermore, the heavily overconsolidated clay does not contract. However, for dense sand, it contracts before dilation.

In order to model the differences between clay and sand, the following extensions have been made in the present micromechanics model: (1) the deformation between clay-clusters due to compression is much bigger than sand. Thus, in addition to the Mohr–Coulomb's plastic shear sliding, a plastic normal deformation has been considered for two clusters in compression. (2) A dilatancy type flow rule accounting for soil density is proposed to reproduce the clay behaviour.

In order to have a general model applicable to various stress paths including both compression and extension loads, we have incorporated a formulation, similar to that used in kinematic hardening rules, Masing's rule or bounding surface (Dafalias and Herrmann, 1982), which can analyse the reverse shear loading condition on a contact plane. With this new element, the model can simulate correctly the extension tests followed anisotropic consolidation.

Experimental results obtained from LCT (Lower Cromer Till) and kaolin clay were adopted for evaluating the model applicability to soils under a K_0 consolidation followed by a drained or undrained shearing. In Section 2, we present the model on the basis of a microstructural approach. In Section 3, we compare the model's performance with the measured response. In Section 4, we show the behaviour of contact planes within the assembly. We also discuss the relationship between the contact plane behaviour and the assembly behaviour. Finally, the overall applicability of the present model is evaluated based on the comparison of measured and predicted results.

2. Constitutive model

A clay particle is usually platy in shape. The size for a platy particle generally ranges from 0.01 to 1 μm depending on the clay type (e.g. Montmorillonite, Illite or Kaolinite). Clay particles attract each other due to surface forces among particles such as chemical, electrostatic, van der Waals forces, etc. These forces pull together the particles to form particle-clusters. The size of the clusters continues to grow until the clusters are large enough so that the cluster weight, due to gravitation, becomes significantly larger than the inter-particle surface forces. At this stage, the cluster looses its potential to attract further clay particles, and the size of clusters stops to grow. The ultimate cluster-size depends on the clay particle type, the liquid inside the pores, and its sedimentation history.

From the photos of clay material under scanning electron microscopes, clusters formed by platy clay particles can be identified as rotund shape, although the microfabric within a cluster may be either a flocculate or dispersed type structure (see Hicher et al., 2000).

At the size of clusters, long-range forces such as electrostatic and van der Waals forces are negligible, and clusters interact with each other mainly through mechanical forces. This explains why sand and clay have similar qualitative behaviour even though each material consists of different constituents (Biarez and Hicher, 1994). Thus clay material, considered as a collection of clusters, can be modelled by analogy to granular material. It is also reasonable to anticipate that the cluster model may not represent the microfabric of all types of clay. Thus the degree of applicability of this model is necessary to be evaluated.

In this model, we envision clay as an aggregate of clusters. The deformation of a representative volume of clay is generated by mobilizing and compressing of all clusters. Thus, the stress–strain relationship can be derived as an average of the deformation behaviour of all local contact planes. For the α^{th} contact plane, the local forces f_j^α and the local movements δ_i^α can be denoted as follows: $f_j^\alpha = \{f_n^\alpha, f_s^\alpha, f_t^\alpha\}$ and $\delta_i^\alpha = \{\delta_n^\alpha, \delta_s^\alpha, \delta_t^\alpha\}$, where the subscripts n, s, and t represent the components in the three directions of the local coordinate system as shown in Fig. 2. The direction outward normal to the plane is denoted as n; the other two orthogonal directions, s and t, are tangential to the plane.

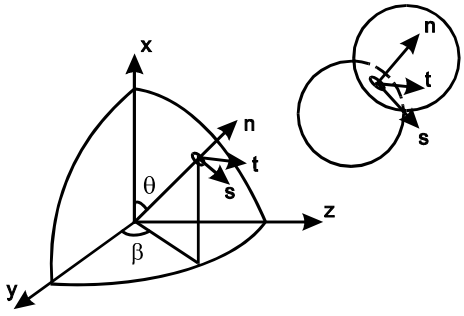

Fig. 2. Local coordinate at inter-particle contact.

2.1. Density state of clay

Critical state concept is important to be considered in the modelling of clay. At critical state, the clay material remains a constant volume while it is subjected to a continuous distortion. The void ratio corresponding to this state is e_c, which is a function of effective mean stress $p' = (\sigma'_x + \sigma'_y + \sigma'_z)/3$. The relationship has traditionally been written as follows:

$$e_c = e_{c0} - \lambda \ln\left(\frac{p}{p_{cr0}}\right). \tag{1}$$

The two parameters (e_{c0}, p_{cr0}) represent a reference point on the critical state line. For convenience, the value of p_{cr0} is taken to be 0.01 Mpa, thus the critical state line can be defined by two parameters e_{c0} and λ. Using the critical state concept, the density state of an assembly is defined as the ratio e_c/e, where e is the void ratio of the assembly.

2.2. Inter-cluster behaviour

In order to have a more apparent link between the micro and macro variables, we define a local stress τ_i^α and a local strain γ_i^α, which are directly related to the local forces f_j^α and the local movements δ_i^α at each contact, given by

$$\tau_i^\alpha = \frac{Nl^\alpha}{3V} f_i^\alpha, \quad \gamma_i^\alpha = \delta_i^\alpha / l^\alpha, \tag{2}$$

where l^α is the length of the branch vector, which joins the centroids of two contact clusters. V is the volume of the representative element. It is to be noted that the local stress τ_i^α is not the stress on the physical contact area between the two clusters. It should be rather viewed as the average stress on the inter-cluster plane when the clusters and voids in the representative volume are homogenized into a continuum. For an isotropic medium, the local stress is identical to the tractions resolved on the plane due to global stress (i.e., $\tau_i^\alpha = \sigma_{ji} n_j^\alpha$). A proof will be given later in Eq. (24).

In the local coordinate system, the local stress and local strain are, respectively, denoted as $\{\tau_n^\alpha \quad \tau_s^\alpha \quad \tau_t^\alpha\}$ and $\{\gamma_n^\alpha \quad \gamma_s^\alpha \quad \gamma_t^\alpha\}$. For convenience, we use the notation $\sigma^\alpha = \tau_n^\alpha$ for local normal stress and the notation $\varepsilon^\alpha = \gamma_n^\alpha$ for local normal strain in the following sections.

2.2.1. Elastic part

The inter-cluster behaviour can be characterized as the relationship between local stress and local strain, given by

$$\tau_i^\alpha = \bar{k}_{ij}^\alpha \gamma_j^\alpha, \tag{3}$$

in which the stiffness tensor can be related to the contact normal stiffness, $\bar{k}_n^\alpha$, and shear stiffness, $\bar{k}_r^\alpha$,

$$\bar{k}_{ij}^\alpha = \bar{k}_n^\alpha n_i^\alpha n_j^\alpha + \bar{k}_r^\alpha (s_i^\alpha s_j^\alpha + t_i^\alpha t_j^\alpha). \tag{4}$$

The inter-cluster stiffness can be expressed as the form adopted for sand grains by Chang et al., 1989), given by

$$\bar{k}_n^\alpha = \bar{k}_{n0}^\alpha \left(\frac{\sigma^\alpha}{p_{ref}}\right)^n, \quad \bar{k}_r^\alpha = k_{rR} \bar{k}_n^\alpha = k_{rR} \bar{k}_{n0}^\alpha \left(\frac{\sigma^\alpha}{p_{ref}}\right)^n, \tag{5}$$

where σ^α is the local stress in normal direction, p_{ref} is the standard reference pressure taken as 0.01 Mpa, and k_{rR} is the ratio of shear to normal stiffness. $\bar{k}_{n0}^\alpha$, k_{rR} and n are material constants. The value of n is found to be 0.33 for two elastic spheres according to Hertz-Mindlin's formulation (1969). Based on experimental measurements of elastic modulus under different confining stress, the value of n have been found to be 0.5–1.0 for clay.

2.2.2. Plastic part

2.2.2.1. Shear sliding. The elastic part of the tangential movement between two clusters does not have a coupling effect (i.e., there is no shear induced normal movements). However, plastic sliding often occurs along the tangential direction of the contact plane with an upward or downward movement (i.e., dilation or contraction). Stress-dilatancy is a well-known phenomenon in sand (see discussions in the work by Taylor (1948), Rowe (1962), Goddard and Bashir (1990), etc.), and should be correctly modelled. The assertion of coupling effect due to plastic sliding of two clusters is not supported by direct observations on the microfabric of actual clay. It is rather a hypothesis presumed from the observed behaviour of soil specimen. The dilatancy equation used here is modified from the equation adopted for sand by Chang and Hicher (2005), given by

$$\frac{d\varepsilon^p}{d\gamma^p} = b\left(\frac{\tan\phi_m}{\tan\phi_\mu} - 1\right)\left(\frac{\tan\phi_m}{\tan\phi_\mu}\right)^a \left(1 - \frac{e}{e_c}\right). \tag{6}$$

The modified equation allows more flexibility for modelling different types of behaviour. In this equation, the mobilized friction angle, $\tan\phi_m = \tau^\alpha/\sigma^\alpha$. The constants a, b and ϕ_μ are inter-cluster properties; e_c is the critical void ratio for the clay. When the void ratio e is equal to the critical void ratio, zero dilation holds. It is noted that the state variables e and e_c are the state of a cluster assembly, which is used to regulate the dilation of individual inter-cluster contacts. It is rational to consider the micro variable as a function of the macro-state, because the inter-cluster behaviour is indeed influenced by the density state of the specimen.

In Eq. (6), ϕ_μ is the inter-cluster friction angle, which in value is very close to the internal friction angle of the clay measured at critical state. The values of a and b can be calibrated from experimental measurements of triaxial tests, which will be shown in the later section on numerical simulation.

Note that the shear stress τ and the rate of plastic shear strain $d\gamma^p$ in Eq. (6) are defined as

$$\tau = \sqrt{\tau_s^2 + \tau_t^2} \quad \text{and} \quad d\gamma^p = \sqrt{(d\gamma_s^p)^2 + (d\gamma_t^p)^2}. \tag{7}$$

The yield function of a contact plane is assumed to be of Mohr–Coulomb type, given by

$$F_1(\tau, \sigma, \kappa_1) = \tau - \sigma\kappa_1(\gamma^p) = 0, \tag{8}$$

where $\kappa_1(\gamma^P)$ is an isotropic hardening/softening parameter. Plastic loading corresponds to $dF_1 > 0$. The hardening parameter is defined by a hyperbolic function in the $\kappa_1 - \gamma^p$ plane, which involves two material constants: ϕ_p and $\bar{k}_p$.

$$\kappa_1 = \frac{\bar{k}_p \tan\phi_p \gamma^p}{\sigma \tan\phi_p + \bar{k}_p \gamma^p}. \tag{9}$$

When plastic deformation increases, κ_1 approaches asymptotically $\tan\phi_p$. For a given value of σ, the initial slope of the hyperbolic curve is $\bar{k}_p/\sigma$. The flow rule is non-associated. Under a loading condition, the shear plastic flow in the direction tangential to the contact plane is determined by a normality rule applied to the yield function. However, the plastic flow in the direction normal to the contact plane is governed by the stress-dilatancy equation in Eq. (6).

The value of $\bar{k}_p$ is found to be linearly proportion to $\bar{k}_n$ such that

$$\bar{k}_p^\alpha = k_{pR} \bar{k}_n^\alpha = k_{pR} \bar{k}_{n0}^\alpha \left(\frac{\sigma^\alpha}{p_{ref}}\right)^n. \tag{10}$$

The ratio k_{pR} is a material parameter.

The internal friction angle ϕ_μ is a constant for a given material. However, the peak friction angle, ϕ_p, on a contact plane is dependent on the density state of neighbouring clusters, which can be related to the void ratio e by

$$\tan\phi_p = \left(\frac{e_c}{e}\right)^m \tan\phi_\mu, \tag{11}$$

where m is a material constant (Biarez and Hicher, 1994).

In a loose structure, clusters can rotate more freely, the peak frictional angle ϕ_p is smaller than ϕ_μ. On the other hand, a dense structure provides higher degree of interlocking, which requires more effort to mobilize the clusters in contact. Thus, the peak frictional angle ϕ_p is greater than ϕ_μ. When the loading stress reaches the peak frictional angle ϕ_p, the dense structure dilates and the degree of interlocking relaxes. As a consequence, the peak frictional angle is reduced, which results in a strain-softening phenomenon.

Upon shear reversal, the direction of sliding of an inter-cluster plane is reversed. Let us denote the stress state on the contact plane at the moment of shear reversal be residual stress, which has a significant influence on the subsequent sliding behaviour. As a consequence, the hardening rule and the dilation follow the equations below:

$$\kappa_1 = \frac{\bar{k}_p \tan\phi_p^* \gamma^{p*}}{\sigma \tan\phi_p^* + \bar{k}_p \gamma^{p*}}, \tag{12}$$

$$\frac{d\varepsilon^p}{d\gamma^p} = b\left(\frac{\tan\phi_m^*}{\tan\phi_\mu^*} - 1\right)\left(\frac{\tan\phi_m^*}{\tan\phi_\mu^*}\right)^a \left(1 - \frac{e}{e_c}\right). \tag{13}$$

Note that these two equations carry the same form as the previous ones. The only difference is the superscript $(^*)$ marked on the plastic shear strain γ^{p*}, the mobilized friction angle ϕ_m^*, the internal friction angle ϕ_μ^*, and the peak friction angle ϕ_p^*, which are defined below to show the effect of the reverse state (see Fig. 3).

$$\gamma^{p*} = \sqrt{(\gamma_s^p - \gamma_s^{pR})^2 + (\gamma_t^p - \gamma_t^{pR})^2}, \tag{14}$$

$$\tan\phi_m^* = \tan\phi_R - \tan\phi_m, \tag{15}$$

$$\tan\phi_\mu^* = \tan\phi_R - \tan\phi_\mu, \tag{16}$$

$$\tan\phi_p^* = \tan\phi_R - \tan\phi_p, \tag{17}$$

where $\tan\phi_R$ is the mobilized friction angle $\tan\phi_m$ at the moment of stress reverse, and $(\gamma_s^{pR}, \gamma_t^{pR})$ are the plastic shear strain at the moment of stress reverse. Both $\tan\phi_R$ and $\tan\phi_m$ are positive when the stresses applied to the sample are in a compression state and negative in an extension state. The value of $\tan\phi_\mu$ is positive when the incremental stresses applied is in a compression state and vise versa.

Eq. (13) indicates that the amount of dilation is different upon shear reversal. This concept is similar to that proposed by Balendran and Nemat-Nasser (1993) and Wan and Guo (2001). Eq. (12) suggests that the same form of hardening rule can be used for both loading and unloading conditions, but requires some scaling process on the values of $\tan\phi_m$ and $\tan\phi_p$. This concept is similar to that used in Masing's rule and in bounding surface (Dafalias and Herrmann, 1982).

2.2.2.2. Normal compression. In order to describe the compressible behaviour between two clay clusters, a second yield surface is added. The second yield function is assumed to be as follows:

$$F_2(\sigma, \kappa_2) = \sigma - \kappa_2(\varepsilon^p) \quad \text{for } \sigma > p_p, \tag{18}$$

where the local normal stress σ and local normal strain ε^p are defined in Eq. (2). The normal plastic strain ε^p is generated from the 2nd yield surface only. The hardening function $\kappa_2(\varepsilon^p)$ is defined as

$$\kappa_2 = \sigma_p 10^{\varepsilon^p/c_p} \quad \text{or} \quad \varepsilon^p = c_p \log\frac{\kappa_2}{\sigma_p}, \tag{19}$$

where c_p is the compression index for the compression curve plotted on $\varepsilon^p - \log\sigma$ plane. When the compression σ is less than σ_p, the plastic strain produced by the second yield function is null. Thus, σ_p in Eq. (12) corresponds to the pre-consolidation stress in soil mechanics.

2.2.3. Elasto-plastic relationship

With the basic elements of inter-cluster behaviour discussed above, the final incremental local stress–strain relation of the inter-cluster contact can be derived that includes both elastic and plastic behaviour, given by

$$\dot{\tau}_i^\alpha = \bar{k}_{ij}^{\alpha p} \dot{\gamma}_j^\alpha. \tag{20}$$

Detailed derivation of the elasto-plastic stiffness tensor is given in Appendix.

2.3. Stress–strain relationship

2.3.1. Macro–micro relationship

The stress–strain relationship for an assembly of clay-clusters can be determined from integrating the inter-cluster behaviour at all contacts. During the integration process, a relationship is required to link the macro and micro variables. Using the static hypotheses proposed by Liao et al. (1997), we obtain the relation between the strain of assembly and inter-cluster strain

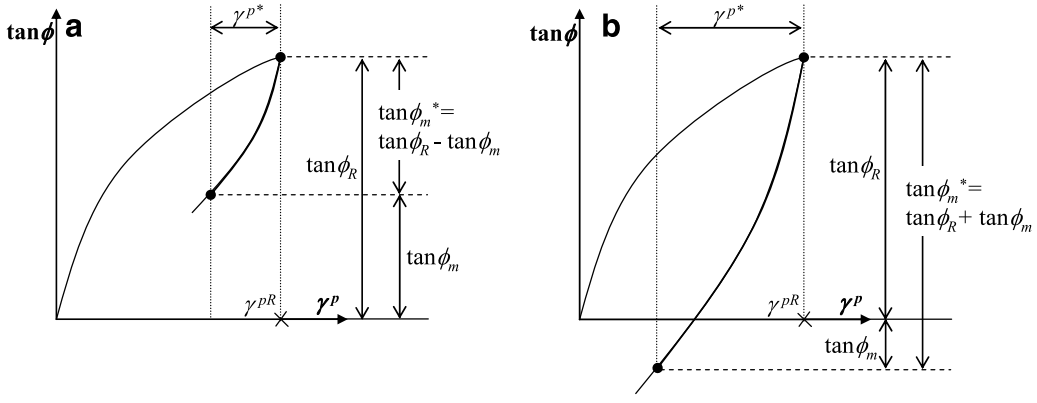

Fig. 3. Stress reversal at loading and unloading.

$$\dot{u}_{j,i} = \sum_{\alpha=1}^{N} \dot{\gamma}_j^{\alpha} n_k^{\alpha} B_{ik}^{\alpha}, \tag{21}$$

where $\dot{\gamma}_j$ is the local strain between two contact clusters; n_k is the unit vector of the branch joining the centres of two contact clusters, and N is the total number of contacts, over which the summation is carried out. The tensor B_{ik}^{α} in Eq. (21) is defined as

$$B_{ik}^{\alpha} = A_{ik}^{-1}(l^{\alpha})^2, \quad \text{where the fabric tensor } A_{ik} = \sum_{\alpha=1}^{N} l_i^{\alpha} l_k^{\alpha} \tag{22}$$

Using the principle of energy balance, which states the work done in a representative volume element equal to the work done on all inter-cluster planes within the element

$$\sigma_{ij}\dot{u}_{j,i} = \frac{1}{V}\sum_{\alpha=1}^{N} f_j^{\alpha}\dot{\delta}_j^{\alpha} = \frac{3}{N}\sum_{\alpha=1}^{N}\tau_j^{\alpha}\dot{\gamma}_j^{\alpha}, \tag{23}$$

and using Eq. (21), the local stress on the α^{th} contact plane is derived as follows:

$$\dot{\tau}_j^{\alpha} = \frac{N}{3}\dot{\sigma}_{ij}B_{ik}^{\alpha}n_k^{\alpha}. \tag{24}$$

For the case of isotropic fabric, it can be derived that $B_{ik} = (3/N)\delta_{ik}$, where δ_{ik} is the kronic delta. Thus, Eq. (24) is reduced to the usual form $\dot{\tau}_j^{\alpha} = \dot{\sigma}_{ij}n_j^{\alpha}$.

The stress increment $\dot{\sigma}_{ij}$ can be obtained by the contact forces and branch vectors for all contacts (Christofferson et al., 1981; Rothenburg and Selvadurai, 1981). In terms of local stress, it is

$$\dot{\sigma}_{ij} = \frac{1}{V}\sum_{\alpha=1}^{N} f_j^{\alpha} l_i^{\alpha} = \frac{3}{N}\sum_{\alpha=1}^{N}\tau_j^{\alpha}n_i^{\alpha}. \tag{25}$$

Applying the defined local stress in Eqs. (24), (25) is unconditionally satisfied.

Using Eqs. (20), (21) and (24), the following relationship between stress and strain can be obtained:

$$\dot{u}_{i,j} = C_{ijmp}\dot{\sigma}_{mp}, \tag{26}$$

where

$$C_{ijmp} = \frac{N}{3}\sum_{\alpha=1}^{N}(\bar{k}_{jp}^{ep})^{-1}n_k^{\alpha}n_n^{\alpha}B_{ik}^{\alpha}B_{mn}^{\alpha}. \tag{27}$$

The summation in Eq. (27) can be expressed by a closed-form solution for some limited conditions such as the elastic modulus of randomly packed equal-size particles (Chang et al., 1995). However, in an elastic–plastic behaviour, due to the non-linear nature of the local constitutive equation, a numerical calculation with an iterative process is necessary to carry out the summation in Eq. (27) (see Chang and Hicher, 2005).

2.4. Summary of parameters

The material parameters are summarized as follows:

(1) Microstructural descriptions (two parameters)
- Contact number per unit volume, N/V and mean cluster size, d.

(2) Inter-cluster properties (nine parameters)
- Inter-cluster elastic constants: $\bar{k}_{n0}$, k_{rR} and n.
- Inter-cluster friction angle: ϕ_{μ} and m($m = 1$ suggested for clays).
- Inter-cluster plastic compression index and plastic shear stiffness ratio: c_p and k_{pR}.
- Dilation constants: a and b.

(3) density state of the assembly (three parameters)
- Critical state for the soil: λ and e_{c0}.
- Reference void ratio, e_0, on the isotropic compression line at $p = 0.01$ Mpa.

The size of a clay cluster d can be estimated from an electron microscopic scanning photograph. The value of N/V is not easy to obtain directly from experiments on clay. According to the experimental data by Oda (1977) for three mixtures of spheres, the contact number per unit volume can be approximately related to the void ratio by

$$\frac{N}{V} = \frac{12}{\pi d^3(1+e)e}. \tag{28}$$

Here, we use this equation as a first-order approximation to estimate N/V for clay by treating d as the mean size of the clay clusters. It is noted that the value of contact number per unit volume changes with void ratio. The evolution is accounted during the deformation process.

3. Experimental verification

3.1. Review of experimental results

The experimental verification is presented herein with reference to the test results on LCT by Gens (1982). The test results have been used by researchers to verify conventional elastic–plastic models with a kinematic hardening of yield surface (e.g. Pestana et al., 2002; Dafalias et al., 2006). LCT is classified as a low plasticity silty-clay, has a liquid limit $w_L = 25\%$ and a plasticity index $I_p = 13\%$. The tests on LCT were all performed on specimens consolidated from a slurry with an initial water content $w = 31\%$. The database includes both drained (compression) and undrained (compression and extension) triaxial shear tests on isotropically and anisotropically consolidated specimens with over-consolidation ratios (OCR) ranging from 1 to 10.

3.2. Calibration of model parameters

The model parameters for LCT were calibrated using an isotropically consolidated undrained triaxial compression test and an isotropic consolidation test, as shown in Fig. 4. Parameter $\lambda = 0.066$ was determined from the slope of the isotropic consolidation curve (see Fig. 4a). The values of e_0 can be determined from the isotropic compression line corresponding to $p_{ref} = 0.01$ Mpa (see Fig. 4a). Similarly, the value of e_{c0} can be determined from the critical state line at $p_{cr0} = 0.01$ Mpa. The inter-particle friction angle ϕ_{μ} can be determined from the slope of the critical state line on p'–q plane. Determined from the undrained triaxial test, $\phi_{\mu} = 30°$ (see Fig. 4c). A typical value of $m = 1$ is used. Other parameters can be obtained by curve fitting as shown in Fig. 4a–f as follows:

(1) Inter-particle elastic constants: $\bar{k}_{n0}$, k_{rR} and n.

The exponent $n = 1$ was selected because it provides a linear κ-line (unloading–reloading curve in e–logp' of consolidation test). The value of $\bar{k}_{n0}$ was determined from the κ-line, as shown in Fig. 4a. The value of k_{rR} was determined from the q–ε_1(deviatoric stress versus axial strain) curve of the undrained compression test at the small strain level (see Fig. 4e).

(2) Inter-particle normal hardening rule: c_p.

The value of c_p was determined from the compression and rebound slopes of the isotropic consolidation line (see Fig. 4a).

(3) Inter-particle shear hardening rule: k_{pR}.

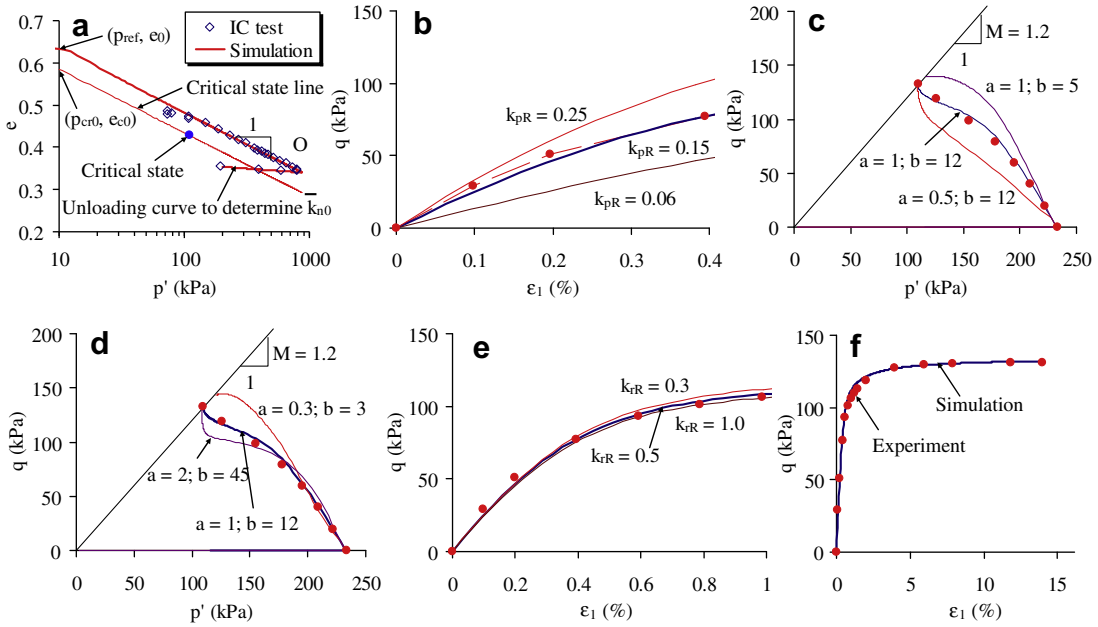

Fig. 4. Calibration of model parameters from isotropic consolidation test and undrained triaxial test.

The value of k_{pR} was determined from the $q - \varepsilon_1$ curve of the undrained compression test at the small strain level, as shown Fig. 4b.

(4) Dilation constants a and b have a significant influence on the shape of undrained stress path. They were determined from the undrained compression test (see Fig. 4c–d). Fig. 4c shows the effect of a (for $b = 12$), and the effect of b (for $a = 1$) on the shape of undrained stress path. In Fig. 4d, three values of a were selected (i.e., 0.3, 1, and 2). For each value of a, we tried to best fit the measured undrained stress path by choosing the most suitable value of b. By the trial and error process, $a = 1$ and $b = 12$ were selected. It is Worth pointing out that the undrained stress path varies it shape for different value of a and b (see Fig. 4c–d), which implies that the proposed dilatancy flow rule can describe different shapes of yield surface.

The model parameters for LCT are listed in Table 1. Using this set of parameters, the q–ε_1 curve was predicted in Fig. 4f, which, as expected, shows a good fit with the experimental curve.

3.3. Undrained shear behaviour

3.3.1. Different K_0 (OCR = 1)

The parameters in Table 1 were calibrated from an undrained compression test on an isotropically consolidated sample. Here, we examine whether the same set of parameters can predict the behaviour of anisotropically consolidated samples under both compression and extension tests. For this purpose, several triaxial tests were simulated. The samples were first anisotropically consolidated with four different consolidation stress ratio K_0 (i.e., the ratio of radial to axial stress σ'_r/σ'_a): 0.4, 0.5, 0.67, and 0.8. Then, for each K_0, two subsequent undrained tests were simulated; a compression test (with an increase of the axial stress while keeping the radial stress constant) and an extension test (with a decrease of the axial stress while keeping the radial stress constant). For all the eight stress paths mentioned above, Fig. 5 shows a good agreement between the numerical and the experimental results using the parameters given in Table 1. The extension test for $K_0 = 0.67$ was predicted without reverse plasticity, and plotted the results in Fig. 5a. The prediction show significant differences from that using reverse plasticity, which demonstrates the necessity of using reverse plasticity in the proposed model.

A peculiar behaviour to be noted is the softening response in the undrained compression tests for the two cases with higher K_0 consolidation (see $K_0 = 0.4$ and 0.5 in Fig. 5). The same form of softening response has often been observed in other types of clay (e.g., Boston blue clay by Ladd and Varallyay (1965); reconstituted London clay by Jardine (1985); Northamption clay by Sambhandharaksa (1977), etc.). The measured softening response cannot be attributed to the destructuration process since the tested clays are reconstituted in many studies mentioned above. This form of softening response is difficult to be modelled by the conventional methods using kinematic hardening of a yield surface (e.g., Wheeler et al., 2003; Ling et al., 2002). However, using specific rotational kinematic hardening rules and yield surface shapes, Pestana et al. (2002) and Dafalias et al. (2006) have managed to simulate the softening response after K_0 consolidation.

In the conventional macro plasticity models based on a critical state framework, the stress state of soil under a large shear strain is located on the critical state line in a stress space (e.g. p–q plane). This can be proscribed by the yield surface and its kinematic hardening rule. The corresponding void ratio of soil is governed by the

Table 1
Values of model parameters for LCT and Kaolin clay.

	Global parameters					Inter-particle parameters				
	e_0	λ	e_{c0}	a	b	c_p	ϕ'_μ (°)	$\bar{k}_{n0}$(Mpa)	k_{rR}	k_{pR}
LCT	0.64	0.066	0.583	1	12	0.026	30	400	0.5	0.15
Kaolin	2.42	0.26	2.21	1	12	0.048	23	150	0.5	0.2

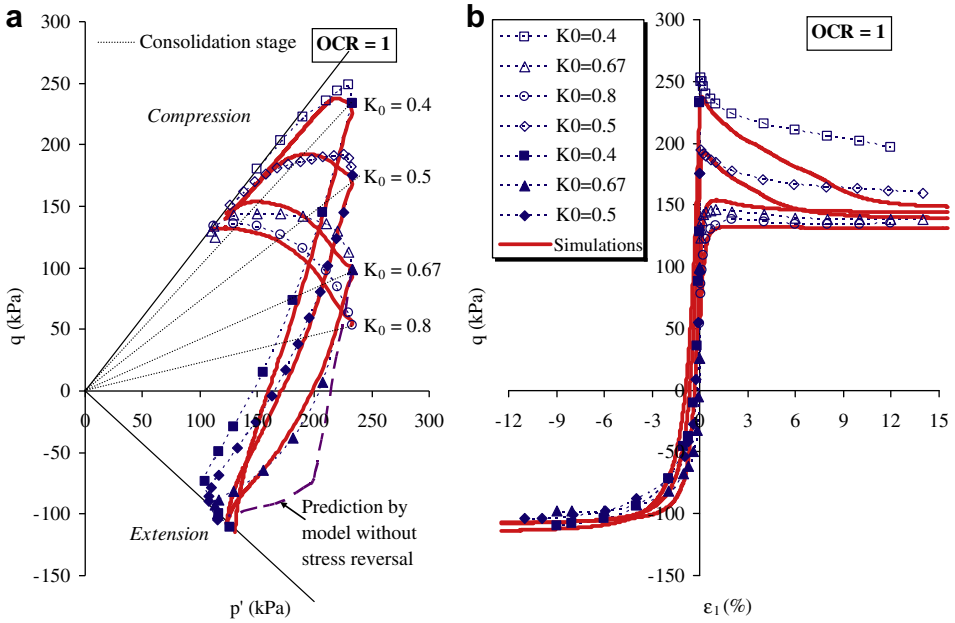

Fig. 5. Comparison between experimental and numerical results for undrained triaxial tests on anisotropically consolidated samples of LCT with OCR = 1.

position of yield surface at this instant, thus is not necessarily equal to the critical state void ratio.

For the conventional macro plasticity models with an isotropic hardening rule, the critical state void ratio may be reached for an isotropically consolidated sample under a large shear strain. But, for a K_0 consolidated sample under a large shear strain, the predicted void ratio would not be equal to the critical void ratio.

For the conventional macro plasticity models with a kinematical hardening rule, in the case of a K_0 consolidated sample under a large shear strain, the predicted void ratio may be equal to the critical state void ratio if the prescribed kinematic rule can move the yield surface to the right position. Since the kinematic rule is usually dependent solely on applied stress, the same rule may not work for clays with different properties (e.g., soft or stiff clays).

Different from the approach via kinematic hardening of a yield surface, the proposed micromechanical approach employs the state variable of density e_c/e (e_c is the void ratio of critical state). This assures the void ratio as well as the stress approach the critical state simultaneously, for clays with any properties and under any stress paths.

At a large shear strain, the stress state tends to be on the critical state line. Thus, the magnitude of mean effective stress p' is governed by the location of the critical state line (on the e–log p' plane). The void ratio also approaches the critical state, thus the shear strength q (on the p'–q plane) is determined from the p' corresponding to the critical state e_c (see the schematic plot in Fig. 6). As a consequence, the softening response is reasonable to occur when the deviatoric stress at the end of K_0 consolidation is higher than the shear strength determined from the critical state line.

3.3.2. Different OCR (K_0 = 0.5)

Simulations have also been carried out to evaluate the model's performance for predicting the effects of OCR. The samples were first anisotropically consolidated under K_0 = .5 up to $\sigma'_a = 350$ kPa. Then, the samples were unloaded along a different stress path to four different over-consolidation ratios, OCR = 1, 2, 4, 7 (see the dotted line in Fig. 7a). For each OCR, two subsequent undrained tests were simulated; a compression test and an extension test. Fig. 7 shows the comparisons between the experimental data and the model predictions for undrained triaxial tests with

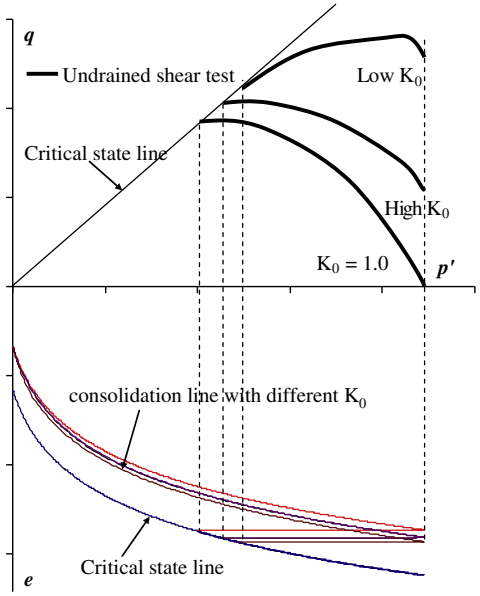

Fig. 6. Schematic plot for undrained compression behaviour with different K_0 consolidation by the proposed model.

four different OCRs. The comparisons in Fig. 7 indicate a good agreement in the major features of the undrained behaviour for samples with different OCRs. The predicted shear strengths for the compression tests (OCR = 4 and 7), however, are lower than those of the experimental ones (see Fig. 7b).

3.4. Drained shear behaviour

3.4.1. Different K_0 (OCR = 1)

Four drained triaxial compression tests are also selected for simulation. After being consolidated to different values of K_0 (0.4, 0.5, 0.67, 1.0), the samples are loaded to failure in a drained condition as the stress paths shown in Fig. 8a. Fig. 8 shows a good agreement between the numerical and the experimental results of

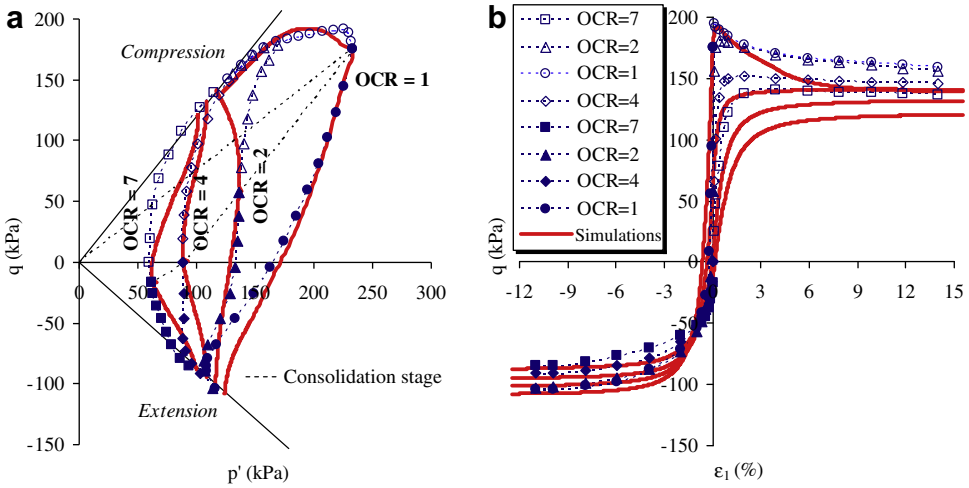

Fig. 7. Comparison between experimental and numerical results for undrained triaxial tests on anisotropically consolidated samples of LCT with various OCR from 1 to 7.

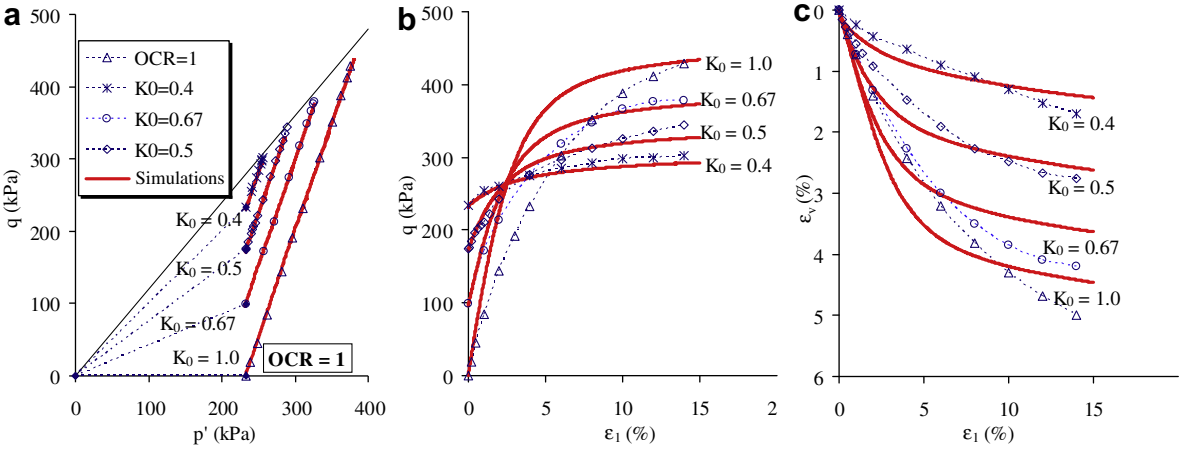

Fig. 8. Comparison between experimental and numerical results for drained triaxial tests on anisotropically consolidated samples of LCT with OCR = 1.

drained triaxial tests, using the set of parameters determined from an undrained test (Table 1). The measured volumetric strain increases with the value of K_0, whereas the shear strength decreases with the value of K_0. The model prediction reflects the measured trends of behaviour.

3.4.2. Different OCRs (K_0 = 0.5)

Fig. 9 shows the comparisons between the experimental data and the model predictions for drained K_0-consolidated specimens with different *OCRs*. Similar to the undrained tests, the samples were first anisotropically consolidated under K_0 = .5, then unloaded

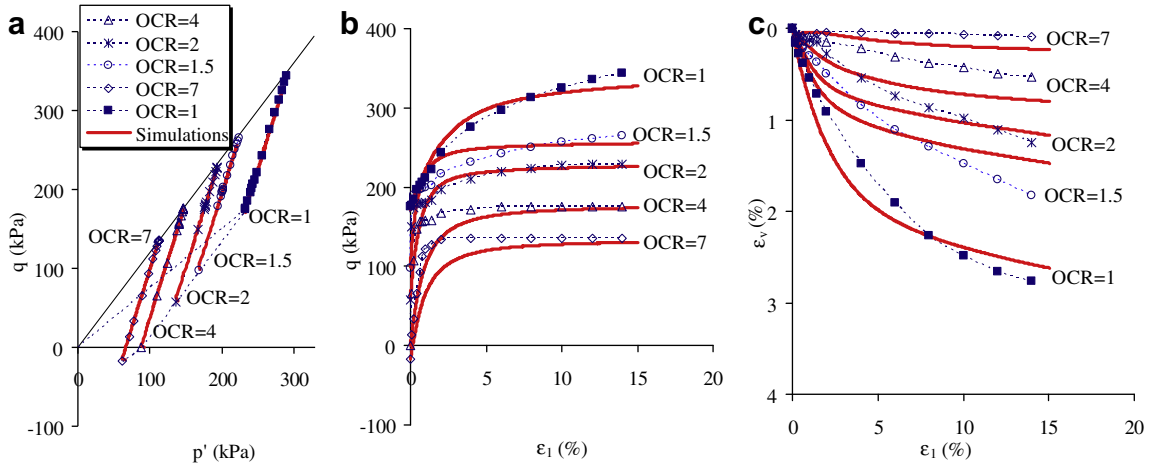

Fig. 9. Comparison between experimental and numerical results for drained triaxial tests on anisotropically consolidated samples of LCT with various OCR from 1 to 7.

to different values of *OCR* (1, 1.5, 2, 4, and 7) through a different stress path as the dotted line shown in Fig. 9a. Subsequently, the samples are followed by an increase of axial load until the vertical strain is 15%. The trends of shear strength and volume change for samples with different values of OCR are also reproduced by the present model using the same set of parameters in Table 1.

Overall, although there are discrepancies between experiments and simulations, the model simulations in general have a better fit to the experimental results than the simulations on the same tests predicted from models by Pestana et al. (2002) and Dafalias et al. (2006).

3.5. Test simulations for kaolin

In order to evaluate the model applicability on a true (non-natural) clay, undrained triaxial tests on saturated kaolin performed by Wroth and Loudon (1967) were used. The selected tests were performed on kaolin specimens with isotropic consolidation under different OCRs from 1 to 6.5.

The result of isotropic consolidation tests is shown in Fig. 10. The critical state line in Fig. 10 was obtained from the undrained compression test on normally consolidated sample. Similar to the calibration procedure of model parameters for LCT, all parameters for kaolin can be determined using two standard tests, namely (1) an undrained compression test on an isotropically consolidated sample (OCR = 1), and (2) an isotropic consolidation test. The values of parameters are summarized in Table 1. Fig. 11 shows the comparison between measured and predicted results. The comparisons show that the predicted undrained stress paths represent the behaviour of clay (see Fig. 1) and that the present model gives excellent prediction for tests on all lightly and heavily over-consolidated samples using parameters determined from the tests on normally consolidated samples.

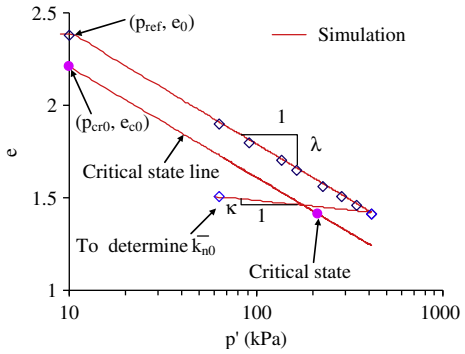

Fig. 10. Isotropic consolidation test for kaolin clay.

4. Micromechanical analysis for induced anisotropy

In this section, we investigate the predicted local stress–strain behaviour for contact planes. Since the applied loading is axi-symmetric about *x*-axis, the orientation of a given contact plane can be represented by inclined angle, θ, which is measured between the branch vector and the *x*-axis of the coordinate system as shown in Fig. 2. Seven contact planes selected for this investigation have inclined angles $\theta = 0°$, 18°, 28°, 45°, 55°, 72°, and 90° ($\theta = 0°$ corresponds to a horizontal contact plane), as shown, respectively, in the *x*–*z* plane in Fig. 12a. The local behaviour of contact planes discussed here includes both undrained (Fig. 12b) and drained conditions (Fig. 12c). Six tests are examined: (1) undrained compression; $K_0 = 0.5$, OCR = 1, (2) undrained compression; $K_0 = 0.5$, OCR = 7, (3) undrained extension; $K_0 = 0.5$, OCR = 1, (4) undrained extension; $K_0 = 0.5$, OCR = 7, (5) drained compression; $K_0 = 0.5$, OCR = 1, and

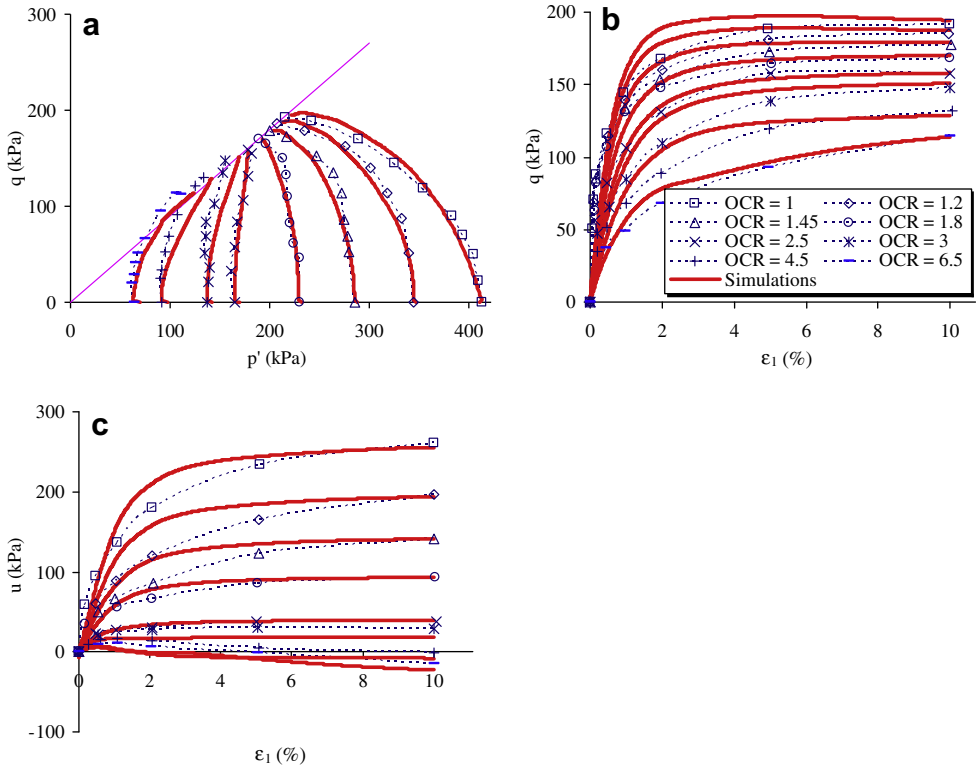

Fig. 11. Comparison between experimental and numerical results for undrained triaxial tests on isotropically consolidated samples of Hong Kong marine clay with various OCR from 1 to 8.

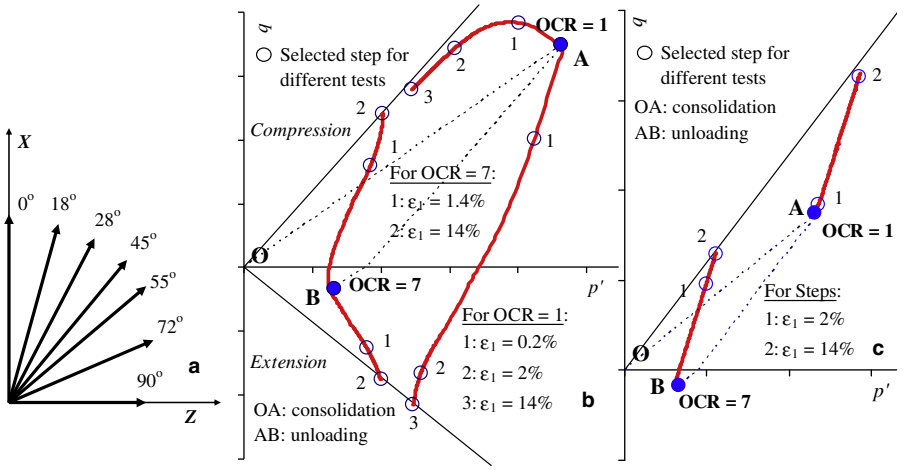

Fig. 12. (a) Five inter-particle orientations located on the *X–Z* plane of the coordinate system, and (b, c) selected steps for rose diagram.

(6) drained compression; $K_0 = 0.5$, OCR = 7. In order to study the evolution of local stresses and strains, we have, in each test, selected several load steps (see Fig. 12b–c), which are marked by hollow circles with load step numbers.

4.1. Undrained condition

4.1.1. Local stress–strain behaviour

We plot the simulated compression and extension test results in Fig. 13a and b for OCR = 1, and in Figs. 13 and 10c and d for OCR = 7. The local stress paths for the seven selected contact orientations are plotted in Fig. 13a and c. In order to show the stress reversal for individual planes, we have added the simulated curves of consolidation stage (see the dotted lines in Fig. 13a). For both cases (OCR = 1 and 7), the stress state closest to the internal friction line is on the 55° contact plane for the compression test and on the 28° contact plane for the extension test. Fig. 13b and d shows local shear stress–strain curves, which clearly indicates that every contact plane is mobilized to a different degree. The planes with largest movements are near the orientation of 55° (close to $\pi/4 + \phi_\mu/$

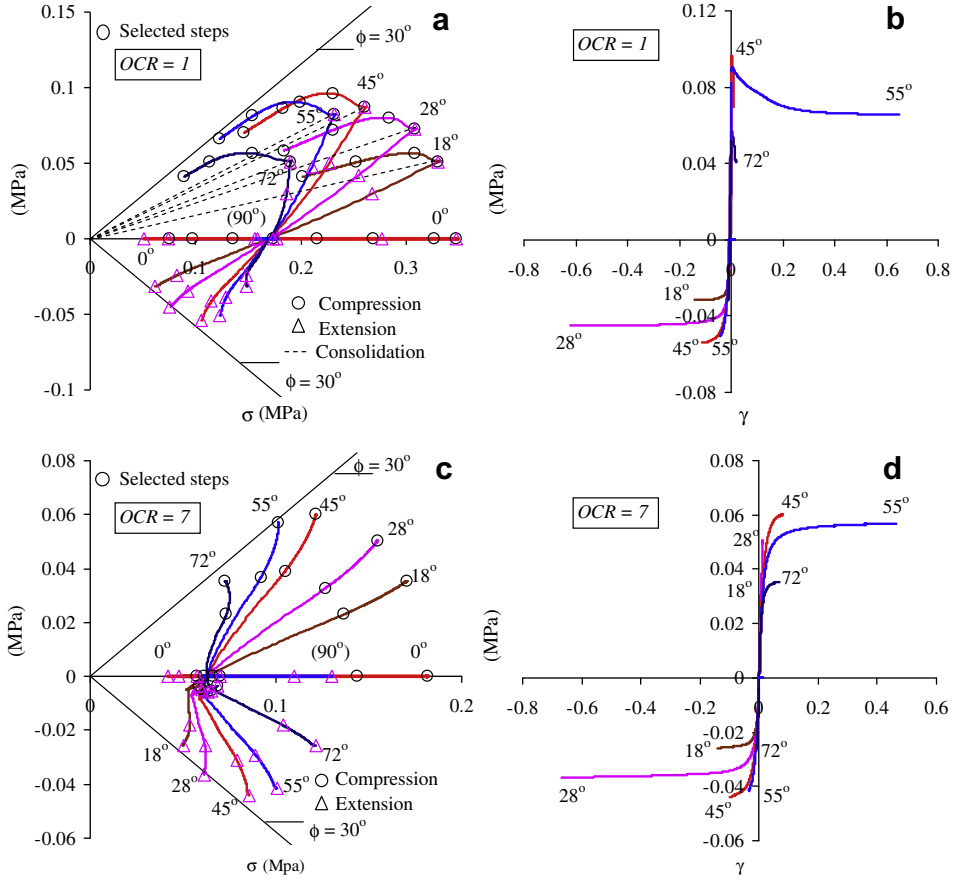

Fig. 13. Local behaviour on seven different inter-particle planes for undrained triaxial test.

$2 = 60°$) for undrained compression tests and of 28° (close to $\pi/4 - \phi_\mu/2 = 30°$) for undrained extension tests. These active contact planes contribute largely to the overall deformation of the specimen. Among the cases in Fig. 13, only the contact planes in the compression test with OCR = 1 exhibit strain-softening phenomenon, which agrees with the overall behaviour shown in Fig. 7.

4.1.2. . Orientation distributions of local stresses and strains

Fig. 14 shows the distributions of local stresses and strains on planes of different orientations (in rose diagram). They are plotted for the ending step of K_0 consolidation (see points A and B in Fig. 12b), and for the selected steps (see hollow circles in Fig. 12b). The stress-induced anisotropy is discussed by comparing the distributions between the compression and the extension tests. The distributions between OCR = 1 and 7 are also compared to highlight the effect of stress history.

4.1.2.1. Compare compression and extension tests with OCR = 1 (series 1C and 1E in Fig. 14). (1) The distribution of *normal stress* σ at the end of K_0 consolidation (corresponding to step A in Fig. 12b) has a long axis in the vertical direction (see the bold line in Fig. 14-1C-a and 1E-a). As oppose to the circular distribution due to the isotropic consolidation (dash line remarked as "case of IC" in Fig. 14-1C-a), the shape of bold line clearly indicates a material anisotropy since the soil properties are stress-dependent. Subsequent to the K_0 consolidation, the distribution shrinks from step A to load step 3 and remains its long axis in the vertical direction during the undrained compression (Fig. 14-1C-a), whereas the distribution changes its long axis from the vertical direction to the horizontal direction during the undrained extension (Fig. 14-1E-a). Thus, the major axis of material anisotropy does not coincide with the major axis of applied stress – a non-coaxial condition has occurred in the undrained extension test.

(2) The distribution of *shear stress* τ at the end of K_0 consolidation is also plotted in bold line as shown Fig. 14-1C-b and 1E-b. Subsequent to the K_0 consolidation, the distribution expands from step A to load step 1 and then shrinks from load step 1 to load step 3 during the undrained compression, whereas the distribution shrinks from step A to load step 1 and continues to shrink until the distribution becomes a point at the origin, followed by expanding into the opposite region from load step 1 to load step 3 (see dash line in Fig. 14-1E-b, here we plot dash line only for the region $0° \leqslant \theta \leqslant 90°$ to emphasize the evolution) during the undrained extension. This signifies that the shear stresses on contact planes have reversed their directions.

(3) The distribution of *stress ratio* τ/σ at the end of K_0 consolidation is shown as the bold line in Fig. 14-1C-c and 1E-c. Subsequent to the K_0 consolidation, the distribution expands from step A to step 3 and remains the same shape during the undrained compression, whereas during undrained extension it shrinks from step A to step 1 and then expands into the opposite region from step 1 to step 3 (see dash line in Fig. 14-1E-c, here we plot dash line only for the region $0° \leqslant \theta \leqslant 90°$ to emphasize the evolution). In the undrained extension, both the shape and the major axis of the distribution have been altered.

(4) The distribution of *normal strain* ε at the end of K_0 consolidation is plotted as the bold line in Fig. 14-1C-d and 1E-d. Subsequent to the K_0 consolidation, strains during the undrained compression decrease slightly for the contact planes with $\theta < 45°$, increase for the contact planes with θ between 45° and 72° due to the dilation (shear induced normal strain) and decrease for the contact planes with $\theta > 72°$ due to the reduction of normal stress. Whereas during the undrained extension strains decrease for the contact planes with $\theta < 45°$ due to a reduction of normal stress, and have very small changes for the contact planes with $\theta > 45°$.

(5) The distribution of *shear strain* γ in Fig. 14-1C-e shows that very large strains have occurred at step 3 within a narrowly oriented band near the orientation of 55° for undrained compression (Fig. 14-1E-e), while very large strains have occurred near the orientation of 28° for undrained extension, which agrees with the located active planes in Fig. 13b.

4.1.2.2. Compare compression and extension tests with OCR = 7 (series 7C and 7E in Fig. 14). (1) The distribution of *normal stress* σ at the end of K_0 consolidation is marked as step A (OCR = 1). The sample is then unloaded from step A to step B (OCR = 7, see the dotted line in Fig. 12b). This unloading process results in a size reduction of the distribution and a change of the shape from a long axis in the vertical direction to the horizontal direction (see Fig. 14-7C-a and 7E-a). Subsequently, during the undrained compression, the distribution expands from step B to step 2 with a change of the long axis from the horizontal direction back to the vertical direction (Fig. 14-7C-a). Whereas, during the undrained extension, the distribution expands from step B to step 2 keeping the long axis in the horizontal direction (Fig. 14-7E-a).

(2) After the end of K_0 consolidation, the distribution of *shear stress* τ is reduced to a very small size during the unloading process from step A to step B (see Fig. 14-7C-b and 7E-b). Subsequently, during both the undrained compression and the undrained extension, the distribution expands from step B to step 2, which agrees with the local stress path in Fig. 12c where the magnitude of shear stress increases for both compression and extension conditions.

(3) After the end of K_0 consolidation, the distribution of *stress ratio* τ/σ is reduced to a very small size during the unload process from step A to step B (see Fig. 14-7C-c and 7E-c). Subsequently, the distribution expands from step B to step 2 with almost the same shape during the undrained compression, whereas during the undrained extension the distribution expands from step B to step 2 with the shape of distribution altered.

(4) After K_0 consolidation, the distribution of *normal strain* ε is moderately reduced in size during the unloading process from step A to step B (see Fig. 14-7C-d and 7E-d). Subsequently, during the undrained compression, strains increase for the contact planes with $\theta < 45°$ and change slightly for those with other θ angles. Whereas, during the undrained extension, strains decrease for the contact planes with $\theta < 45°$ and increase for the contact planes with $\theta > 45°$.

(5) Similar to the case OCR = 1, the distribution of *shear strain* γ in Fig. 14-7C-e shows large strains developed from step 1 to step 2 within a narrowly oriented band near $\theta = 55°$ for the undrained compression, while the distribution in Fig. 14-7E-e shows large strains developed within a narrowly oriented band near $\theta = 28°$ for the undrained extension.

4.2. Drained condition

4.2.1. Local stress–strain behaviour

We plot the predicted local stress–strain behaviour for the two drained compression tests shown in Fig. 12c (see Fig. 9 for the measured test results with OCR = 1 and 7). The local stress paths in Fig. 15a (OCR = 1) and Fig. 15c (OCR = 7) show different slopes from one contact plane to another. Under an increase of the vertical stress, the planes oriented near horizontal direction (i.e., small values of θ) are subjected mainly to a normal stress component $\Delta\sigma$. The shear component becomes more significant when the planes are inclined. The local shear stress–strain curves (Fig. 15b and d) show that every plane is mobilized to a different degree. For both cases of OCR = 1 and 7, the contact plane with largest movement

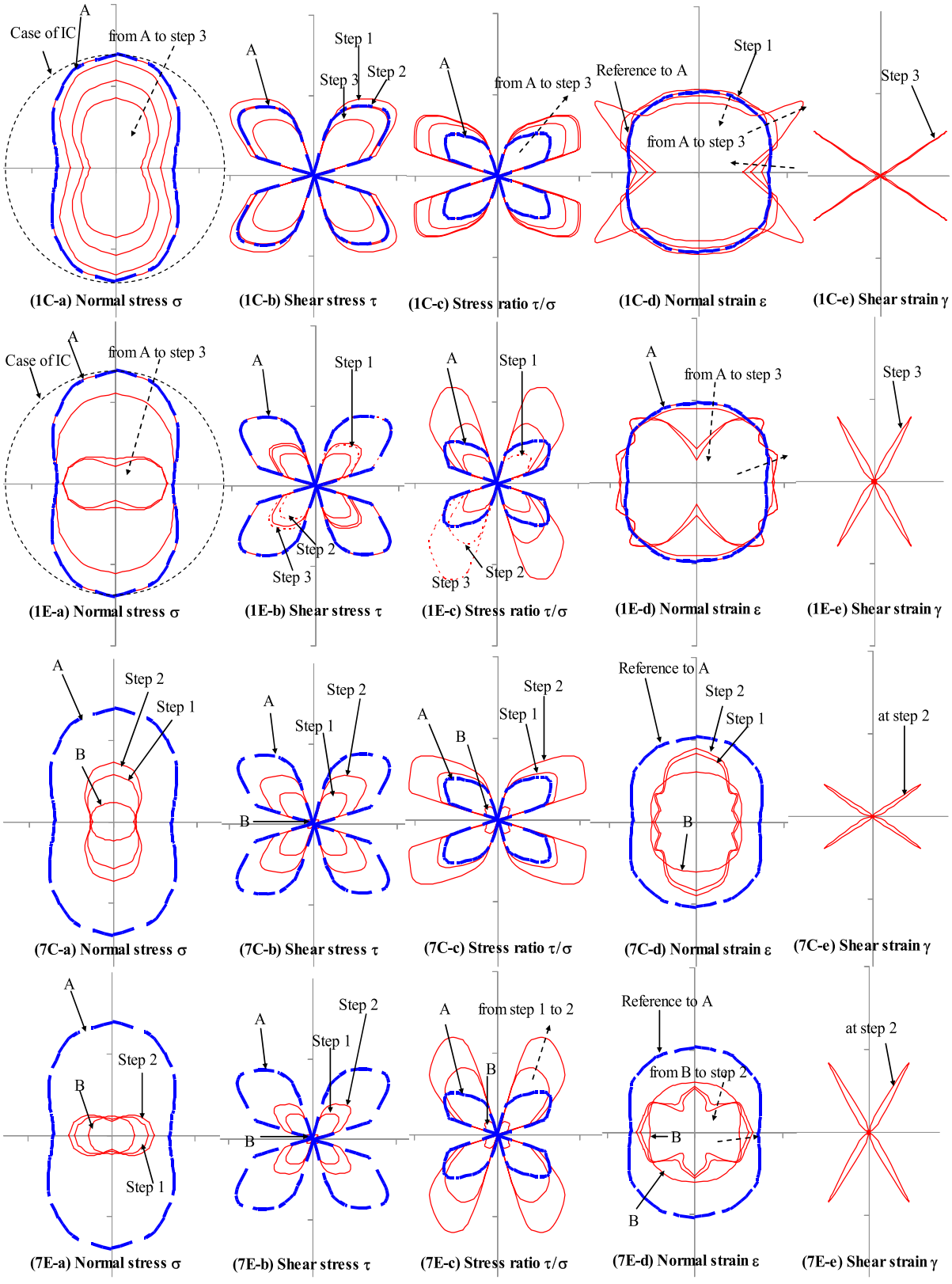

Fig. 14. Schematic plot for induced anisotropy.

has an orientation of 55°, similar to the behaviour observed in the undrained compression case. Other planes are inactive with small movement. It clearly indicates that the local strains do not uniformly conform to the overall strain of the specimen.

4.2.2. . Orientation distributions of local stresses and strains

Fig. 16 shows the distributions of local stresses and strains for contact planes of different orientations (in rose diagram). They are plotted for the end step of K_0 consolidation and for the selected

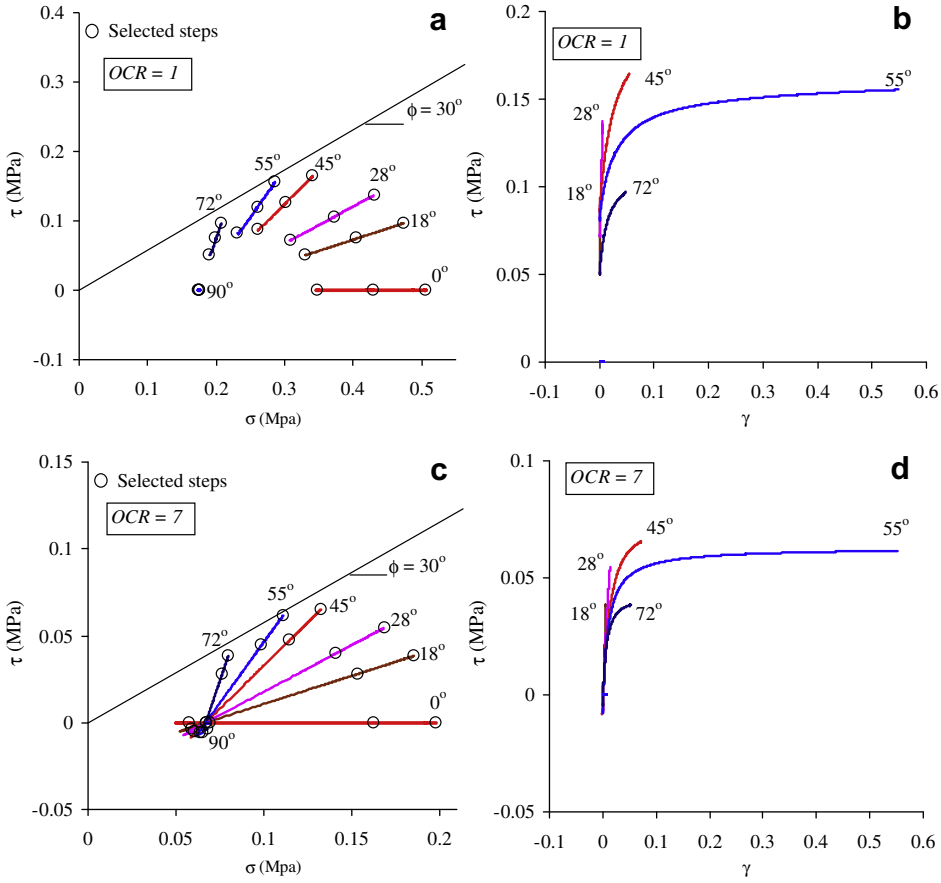

Fig. 15. Local behaviour on seven different inter-particle planes for drained triaxial test.

load steps (see Fig. 12c, *A* for OCR = 1 and *B* for OCR = 7). The comparisons of the distributions (for OCR = 1 and 7) are discussed to highlight the effect of stress history.

4.2.2.1. Compare drained tests with OCR = 1 and OCR = 7 (series 1D and 7D in Fig. 16). (1) The distribution of *normal stress* σ at the end of K_0 consolidation has a long axis in the vertical direction (see the bold line in Fig. 16-1D-a). During the subsequent drained compression, the distribution expands from step A to step 2 keeping the long axis in the vertical direction. The change of normal stresses is negligible for the contact planes with $\theta = 90°$. Whilst for the case of OCR = 7 (Fig. 16-7D-a), the unloading process from step A to step B (OCR = 7) results in a reduction of the distribution size and a change of the distribution shape with a long axis from the vertical direction to the horizontal direction (see Fig. 16-7D-a). During the subsequent drained compression, the distribution expands from step B to step 2 with a change in the long axis from the horizontal direction back to the vertical direction.

(2) After K_0 consolidation, the distribution of *shear stress* τ (see the bold line in Fig. 16-1D-b), expands from step A to step 2 during the drained compression for OCR = 1. Whilst for the case of OCR = 7, the unloading process from step A to step B (OCR = 7) results in a very small size of the distribution (see Fig. 16-7D-b). During the subsequent drained compression, the distribution expands from step B to step 2.

(3) The distributions of *stress ratio* τ/σ for both cases OCR = 1 and 7 are similar to that of shear stress τ.

(4) After K_0 consolidation, the distribution of *normal strain* ε (see the bold line in Fig. 16-1D-d at step A for OCR = 1) indicates a very small change in strains for contact planes with $\theta = 90°$, whereas the distribution shows an increase of strains for all other contact orientations due to not only the compression of normal stress but also the shear induced contraction. For the case of OCR = 7, the unloading process from step A to step B results in a size reduction of the distribution (see Fig. 16-7D-d). During the subsequent drained compression, the distribution expands from step B to step 2. The changes of the distribution are different from that of OCR = 1 because the normal strains in this case deform elastically. It is noted that the stresses are within the elastic limits shown by the bold line.

(5) The distribution of *shear strain* γ (in Fig. 16-1D-e and 7D-e) shows very large strains developed from step 1 to step 2 within a narrowly oriented band near the orientation of 55° for both cases of OCR = 1 and 7.

5. Conclusions and discussions

A new micromechanical stress–strain model has been developed based on the approach proposed by Chang and Hicher (2005). In addition to the Mohr-Coulomb's plastic shear sliding for sand model, a plastic normal deformation has been considered for two clusters in compression. A dilatancy type flow rule accounting for soil density is proposed to reproduce the clay behaviour. The model takes into account the conditions of shear stress reversal on a contact plane. This feature is needed in order for the model to simulate anisotropically consolidated soil samples under compression and extension tests.

A calibration procedure for model parameters has been presented which requires only one undrained triaxial test and one iso-

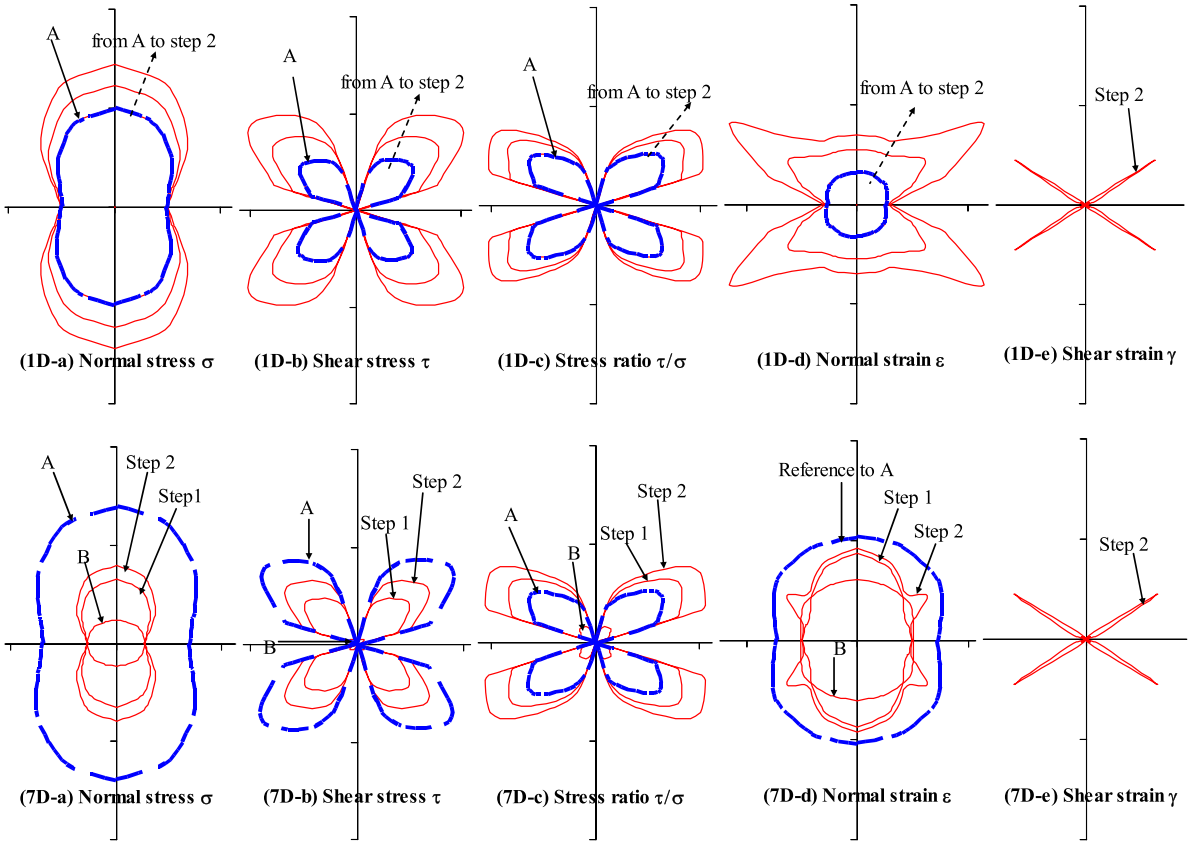

Fig. 16. Schematic plot for induced anisotropy.

tropic consolidation test. The applicability of the model has been examined by comparing the predicted and the measured test results obtained from LCT, including: (a) undrained triaxial compression and extension tests (with $OCR = 1$ but different K_0); (b) undrained triaxial compression and extension tests (with $K_0 = 0.5$ but different OCR); (c) drained triaxial compression tests (with $OCR = 1$ but different K_0); and (d) drained triaxial compression tests (with $K_0 = 0.5$ but different OCR). The predictions of all these tests were performed using one set of parameters. The comparisons between predicted and measured results show reasonably good agreement. The model was further validated by kaolin clay. It is worth pointing out that the present model can predict the undrained softening response of a soil specimen in a compression test following anisotropic consolidation. In the present model, the stresses on each plane are considered as internal state variables, and their evolution can serve to model the behaviour change on each individual plane, thus the results exhibit naturally the stress-induced anisotropy.

The predicted behaviour of contact planes has been examined for soil samples under the triaxial compression and extension tests in both drained and undrained conditions. It has been shown from the rose diagrams that the shape of contact stress distribution changes throughout the triaxial test, which clearly indicates the development of anisotropy induced by the externally applied load, since the properties on each contact plane are stress-dependent. The local stress–strain response on contact planes has shown that every contact plane is mobilized to a different degree. A few active contact planes contribute largely to the deformation of the assembly, while most contact planes are inactive and have small movement. Therefore, the local strains are highly non-uniform.

Model predictions for the LCT and kaolin clay have demonstrated that the present micromechanical approach is capable of modelling the induced anisotropy and the salient features of the complex behaviour in clay. As for future works, the induced anisotropy will be examined for specimens with non-axisymmetric stress states and with rotation of principal axes, such as the experiments in true triaxial tests and hollow cylinder torsional tests.

Appendix. Derivation of $\bar{k}_{ij}^{ep}$

Follow the consistency equation, $dF = 0$, which yield

$$dF = \frac{\partial F}{\partial \tau_i} d\tau_i + \frac{\partial F}{\partial \kappa} \frac{\partial \kappa}{\partial \gamma_i^p} d\gamma_i^p = 0. \tag{A1}$$

For the specific yield functions given in Eqs. (8) and (18), Eq. (A1) can be expressed as

$$\begin{aligned} dF_1 &= \frac{\partial F_1}{\partial \tau_i} d\tau_i - \frac{\partial \kappa_1}{\partial \gamma^p} \frac{\partial \gamma^p}{\partial \gamma_i^p} d\gamma_i^p = 0, \\ dF_2 &= \frac{\partial F_2}{\partial \tau_i} d\tau_i - \frac{\partial \kappa_2}{\partial \varepsilon^p} \frac{\partial \varepsilon^p}{\partial \gamma_i^p} d\gamma_i^p = 0. \end{aligned} \tag{A2}$$

The derivatives in Eq. (A2) can be obtained from the definition of F_1, F_2, κ_1, κ_2, γ^p and ε^p (plastic normal strain produced by the 2nd yield surface) previously defined. The incremental plastic strain has two components generated from the 1st and the 2nd yield surfaces, respectively, as follows:

$$d\gamma_j^p = d\gamma_j^{p,1} + d\gamma_j^{p,2}. \tag{A3}$$

For the first component, we define the plastic flow vector ξ_j^1 such that

$$d\gamma_j^{p,1} = \lambda_1 \xi_j^1. \tag{A4}$$

For this yield surface, the plastic shear strain is obtained in accordance with the associated flow rule (i.e., $d\gamma_j^{p,1} = \lambda_1(\partial F_1/\partial\tau_j)$), but the plastic normal strain is obtained from the dilatancy equation given in Eq. (6). In a vector form

$$\begin{Bmatrix} d\gamma_n^{p,1} \\ d\gamma_s^{p,1} \\ d\gamma_t^{p,1} \end{Bmatrix} = \lambda_1 \begin{Bmatrix} b\left(\frac{\tau/\sigma_n}{\tan\phi_\mu} - 1\right) & \left(\frac{\tau/\sigma_n}{\tan\phi_\mu}\right)^a & \left(1 - \frac{e}{e_c}\right) \\ & \sigma_s/\tau & \\ & \sigma_t/\tau & \end{Bmatrix}, \tag{A5}$$

where $\lambda_1 = d\gamma^p$, which is the scalar plastic strain defined in Eq. (7).

For the second component, we define the plastic flow vector ξ_j^2 such that

$$d\gamma_j^{p,2} = \lambda_2 \xi_j^2. \tag{A6}$$

The plastic strain is obtained in accordance with the associated flow rule (i.e., $d\gamma_j^{p,2} = \lambda_2(\partial F_2/\partial\tau_j)$). In a vector form

$$\begin{Bmatrix} d\gamma_n^{p,2} \\ d\gamma_s^{p,2} \\ d\gamma_t^{p,2} \end{Bmatrix} = \lambda_2 \begin{Bmatrix} 1 \\ 0 \\ 0 \end{Bmatrix}, \tag{A7}$$

where $\lambda_2 = d\gamma_n^{p,2} = d\varepsilon^p$, which is the compressive plastic strain defined in Eq. (18).

Then, Eq. (A3) can be expressed as follows:

$$d\gamma_j^p = \lambda_1 \xi_j^1 + \lambda_2 \xi_j^2. \tag{A8}$$

The strain is assumed to consist of elastic component and plastic component. The stress can be calculated from the elastic component by

$$d\tau_i = \bar{k}_{ij}^e (d\gamma_j - d\gamma_j^p). \tag{A9}$$

Substitute Eq. (A8) to Eq. (A9)

$$d\tau_i = \bar{k}_{ij}^e (d\gamma_j - \lambda_1 \xi_j^1 - \lambda_2 \xi_j^2). \tag{A10}$$

Then substitute Eqs. (A10) and (A8) to Eq. (A2)

$$\begin{cases} dF_1 = \frac{\partial F_1}{\partial \tau_i} \bar{k}_{ij}^e (d\gamma_j - \lambda_1 \xi_j^1 - \lambda_2 \xi_j^2) - \frac{\partial \kappa_1}{\partial \gamma^p} \frac{\partial \gamma^p}{\partial \gamma_i^p} (\lambda_1 \xi_j^1 + \lambda_2 \xi_j^2) = 0 \\ dF_2 = \frac{\partial F_2}{\partial \tau_i} \bar{k}_{ij}^e (d\gamma_j - \lambda_1 \xi_j^1 - \lambda_2 \xi_j^2) - \frac{\partial \kappa_2}{\partial \varepsilon^p} \frac{\partial \varepsilon^p}{\partial \gamma_i^p} (\lambda_1 \xi_j^1 + \lambda_2 \xi_j^2) = 0 \end{cases} \tag{A11}$$

$$\Rightarrow \begin{cases} \frac{\partial F_1}{\partial \tau_i} \bar{k}_{ij}^e d\gamma_j - \lambda_1 \left(\frac{\partial F_1}{\partial \tau_i} \bar{k}_{ij}^e \xi_j^1 + \frac{\partial \kappa_1}{\partial \gamma^p} \frac{\partial \gamma^p}{\partial \gamma_i^p} \xi_i^1 \right) - \lambda_2 \left(\frac{\partial F_1}{\partial \tau_i} \bar{k}_{ij}^e \xi_j^2 + \frac{\partial \kappa_1}{\partial \gamma^p} \frac{\partial \gamma^p}{\partial \gamma_i^p} \xi_j^2 \right) = 0 \\ \xi_{i,2} \bar{k}_{ij}^e d\gamma_j - \lambda_1 \left(\xi_i^2 \bar{k}_{ij}^e \xi_j^1 + \frac{\partial \kappa_2}{\partial \varepsilon^p} \frac{\partial \varepsilon^p}{\partial \gamma_i^p} \xi_i^1 \right) - \lambda_2 \left(\xi_i^2 \bar{k}_{ij}^e \xi_j^2 + \frac{\partial \kappa_2}{\partial \varepsilon^p} \frac{\partial \varepsilon^p}{\partial \gamma_i^p} \xi_j^2 \right) = 0 \end{cases}$$

given $\begin{cases} A_1 = \frac{\partial F_1}{\partial \tau_i} \bar{k}_{ij}^e \xi_j^1 + \frac{\partial \kappa_1}{\partial \gamma^p} \frac{\partial \gamma^p}{\partial \gamma_i^p} \xi_i^1, \\ B_1 = \frac{\partial F_1}{\partial \tau_i} \bar{k}_{ij}^e \xi_j^2 + \frac{\partial \kappa_1}{\partial \gamma^p} \frac{\partial \gamma^p}{\partial \gamma_i^p} \xi_j^2, \\ A_2 = \xi_i^2 \bar{k}_{ij}^e \xi_j^1 + \frac{\partial \kappa_2}{\partial \varepsilon^p} \frac{\partial \varepsilon^p}{\partial \gamma_i^p} \xi_i^1, \\ B_2 = \xi_i^2 \bar{k}_{ij}^e \xi_j^2 + \frac{\partial \kappa_2}{\partial \varepsilon^p} \frac{\partial \varepsilon^p}{\partial \gamma_i^p} \xi_j^2. \end{cases}$ Eq. (A11) can be reduced to a matrix form as

$$\begin{bmatrix} A_1 & B_1 \\ A_2 & B_2 \end{bmatrix} \begin{bmatrix} \lambda_1 \\ \lambda_2 \end{bmatrix} = \begin{bmatrix} \frac{\partial F_1}{\partial \tau_i} \bar{k}_{ij}^e d\gamma_j \\ \xi_i^2 \bar{k}_{ij}^e d\gamma_j \end{bmatrix}. \tag{A12}$$

Substituting Eq. (A12) into Eq. (A10), Eq. (A10) can be expressed in a matrix form as follows:

$$\begin{aligned} \{d\tau_i\} &= [\bar{k}_{ij}^e] \left(\{d\gamma_j\} - [\{\xi_j^1\}\{\xi_j^2\}] \begin{Bmatrix} \lambda_1 \\ \lambda_2 \end{Bmatrix} \right) \\ &= \left([\bar{k}_{ij}^e] - [\bar{k}_{ij}^e][\{\xi_j^1\}\{\xi_j^2\}] \begin{bmatrix} A_1 & B_1 \\ A_2 & B_2 \end{bmatrix}^{-1} \begin{bmatrix} \left\{\frac{\partial F_1}{\partial \tau_i}\right\}^T \\ \{\xi_i^2\}^T \end{bmatrix} [\bar{k}_{ij}^e] \right) d\gamma_j \end{aligned} \tag{A13}$$

The incremental stress–strain relationship for two clusters under sliding and compression can be expressed as

$$\{d\tau_i\} = [\bar{k}_{ij}^{ep}]\{d\gamma_j\}, \tag{A14}$$

where

$$[\bar{k}_{ij}^{ep}] = [\bar{k}_{ij}^e] - [\bar{k}_{ij}^e][\{\xi_j^1\}\{\xi_j^2\}] \begin{bmatrix} A_1 & B_1 \\ A_2 & B_2 \end{bmatrix}^{-1} \begin{bmatrix} \left\{\frac{\partial F_1}{\partial \tau_i}\right\}^T \\ \{\xi_i^2\}^T \end{bmatrix} [\bar{k}_{ij}^e]. \tag{A15}$$

References

Balendran, B., Nemat-Nasser, S., 1993. Double sliding model for cyclic deformation of granular materials including dilatancy effects. Journal of Mechanics and Physics of Solids 41 (3), 573–612.

Batdorf, S.B., Budianski, B., 1949. A mathematical theory of plasticity based on concept of slip. NACA Tech Note TN 1871.

Bazant, Z.P., Xiang, Y., Ozbolt, J., 1995. Nonlocal microplane model for damage due to cracking. Proceedings of Engineering Mechanics 2, 694–697.

Biarez, J., Hicher, P.Y., 1994. Elementary Mechanics of Soil Behaviour. Balkema, Rotterdam. 208 pp..

Burland, J.B., 1990. On the compressibility and shear strength of natural clays. Geotechnique 40 (3), 329–378.

Calladine, C.R., 1971. A microstructural view of the mechanical properties of saturated clay. Geotechnique 21 (4), 391–415.

Chang, C.S., Chao, S.C., Chang, Y., 1995. Estimates of mechanical properties of granulates with anisotropic random packing structure. International Journal of Solids and Structures 32 (14), 1989–2008.

Chang, C.S., Hicher, P.Y., 2005. An elastic–plastic model for granular materials with microstructural consideration. International Journal of Solids and Structures 42 (14), 4258–4277.

Chang, C.S., Sundaram, S.S., Misra, A., 1989. Initial Moduli of Particulate Mass with Frictional Contacts. International Journal for Numerical and Analytical Methods in Geomechanics 13 (6), 626–641.

Christofferson, J., Mehrabadi, M.M., Nemat-Nassar, S., 1981. A micromechanical description on granular material behaviour. ASME Journal of Applied Mechanics 48, 339–344.

Cudny, M., Vermeer, P.A., 2004. On the modelling of anisotropy and destructuration of soft clays within the multi-laminate framework. Computers and Geotechnics 31 (1), 1–22.

Dafalias, Y.F., 1986. An anisotropic critical state soil plasticity model. Mechanics Research Communications 13 (6), 341–347.

Dafalias, Y.F., Herrmann, L.R., 1982. Bounding surface formulation of soil plasticity. In: Pande, G.N., Zienkiewicz, D.C. (Eds.), Soil Mechanics – Transient and Cyclic Loads. Wiley, New York, pp. 253–282.

Dafalias, Y.F., Manzari, M.T., Papadimitriou, A.G., 2006. SANICLAY: simple anisotropic clay plasticity model. International Journal for Numerical and Analytical Methods in Geomechanics 30 (12), 1231–1257.

Diaz Rodriguez, J.A., Leroueil, S., Aleman, J.D., 1992. Yielding of Mexico City clay and other natural clays. Journal of Geotechnical Engineering 118 (7), 981–995.

Gens, A., 1982. Stress–strain and strength of a low plasticity clay. Ph.D. Thesis at Imperial College, London University.

Goddard, J.D., Bashir, Y.M., 1990. On Reynolds dilatancy. In: De Kee, D., Kaloni, P.N. (Eds.), Recent Development in Structeured Continua, vol. II. Longman, London, pp. 23–35.

Hicher, P.Y., Wahyudi, H., Tessier, D., 2000. Microstructural analysis of inherent and induced anisotropy in clay. Mechanics of Cohesive-Frictional Materials 5 (5), 341–371.

Jardine, R.J., 1985. Investigations of pile-soil behaviour with special reference to the foundations of offshore structures. Ph.D. Thesis, Imperial College, University of London, London, UK.

Ladd, C.C., Varallyay, J., 1965. The influence of the stress system on the behaviour of saturated clays during undrained shear. Research Rep. No. R65-11, Dept. of Civil Engineering, MIT, Cambridge, MA.

Liao, C.L., Chang, T.P., Young, D., Chang, C.S., 1997. Stress-strain relationship for granular materials bases on hypothesis of best fit. International Journal of Solids and Structures 34 (31–32), 4087–4100.

Ling, H.I., Yue, D., Kaliakin, V.N., 2002. Anisotropic elastoplastic bounding surface model for cohesive soils. Journal of Engineering Mechanics 128 (7), 748–758.

Mindlin, R.D., 1969. Microstructure in linear elasticity. Archive for Rational Mechanics and Analysis 16, 51–78.

Muir Wood, D., 1990. Soil Behaviour and Critical State Soil Mechanics. Cambridge University Press, Cambridge, UK.

Nova, R., 1985. Mathematical modelling of anisotropy of clays. Proceedings of the 11th ICSMFE, San Francisco, vol. 1. Balkema, Rotterdam. pp. 607–661.

Oda, M., 1977. Co-ordination number and its relation to shear strength of granular material. Soils and Foundations 17 (2), 29–42.

Pande, G.N., Sharma, K.G., 1982. Multi-laminate model of clays – a numerical evaluation of the influence of rotation of the principal stress axis. In: Desai, C.S., Saxena, S.K. (Eds.), Proceedings of Symposium on Implementation of Computer Procedures and Stress–strain Laws in Geotechnical Engineering. Acorn Press, Chicago, Durham, NC, pp. 575–590.

Pestana, J.M., Whittle, A.J., 1999. Formulation of a unified constitutive model for clays and sands. International Journal for Numerical and Analytical Methods in Geomechanics 23, 1215–1243.

Pestana, J.M., Whittle, A.J., Gens, A., 2002. Evaluation of a constitutive model for clays and sands: Part II – Clay behaviour. International Journal for Numerical and Analytical Methods in Geomechanics 26 (11), 1123–1146.

Rothenburg, L., Selvadurai, A.P.S., 1981. In: Selvadurai, A.P.S. (Eds.), Micromechanical Definitions of the Cauchy Stress Tensor for Particular Media. Mechanics of Structured Media, Amsterdam, pp. 469–486.

Rowe, P.W., 1962. The stress-dilatancy relations for static equilibrium of an assembly of particles in contact. Proceedings of the Royal Society of London Series A – Mathematical and Physical Sciences 269, 500–527.

Sambhandharaksa, S., 1977. Stress strain strength anisotropy of varved clays. Ph.D. Thesis, Massachusetts Institute of Technology.

Tavenas, F., Lereoueil, S., 1977. Effects of stresses and time on yielding of clays. In: Proc. of the 9th ICSMFE, vol. 1, pp. 319–326.

Taylor, D.W., 1948. Fundamentals of Soil Mechanics. Wiley, NewYork, NY.

Wan, R.G., Guo, P.J., 2001. Drained cyclic behavior of sand with fabric dependence. Journal of Engineering Mechanics 127 (11), 1106–1116.

Wheeler, S.J., Näätänen, A., Karstunen, M., Lojander, M., 2003. An anisotropic elasto-plastic model for soft clays. Canadian Geotechnical Journal 40, 403–418.

Whittle, A.J., Kavvadas, M.J., 1994. Formulation of MIT-E3 constitutive model for overconsolidated clays. Journal of Geotechnical Engineering 120 (1), 173–198.

Wroth, C.P., Loudon, P.A., 1967. The correlations of strains within a family of triaxial tests on overconsolidated samples of kaolin. In: Proc. Geotechn. Conf., Oslo, vol. 1, pp. 159–163.